Operando constructing vanadium tetrasulfide-based heterostructures enabled by extrinsic adsorbed oxygen for enhanced zinc ion storage

Junwei Ding[1], Hongge Gao[1], Wenqing Liu[1], Shiwen Wang[1], Shide Wu[1], Shaoming Fang[1, *], and Fangyi Cheng[2, *]

Henan Provincial Key Laboratory of Surface & Interface Science and College of Materials and Chemical Engineering, Zhengzhou University of Light Industry, Zhengzhou 450002, China. Email: mingfang@zzuli.edu.cn.

Key Laboratory of Advanced Energy Materials Chemistry (Ministry of Education), College of Chemistry, Collaborative Innovation Center of Chemical Science and Engineering, Nankai University, Tianjin 300071, China.
Email: fycheng@nankai.edu.cn.

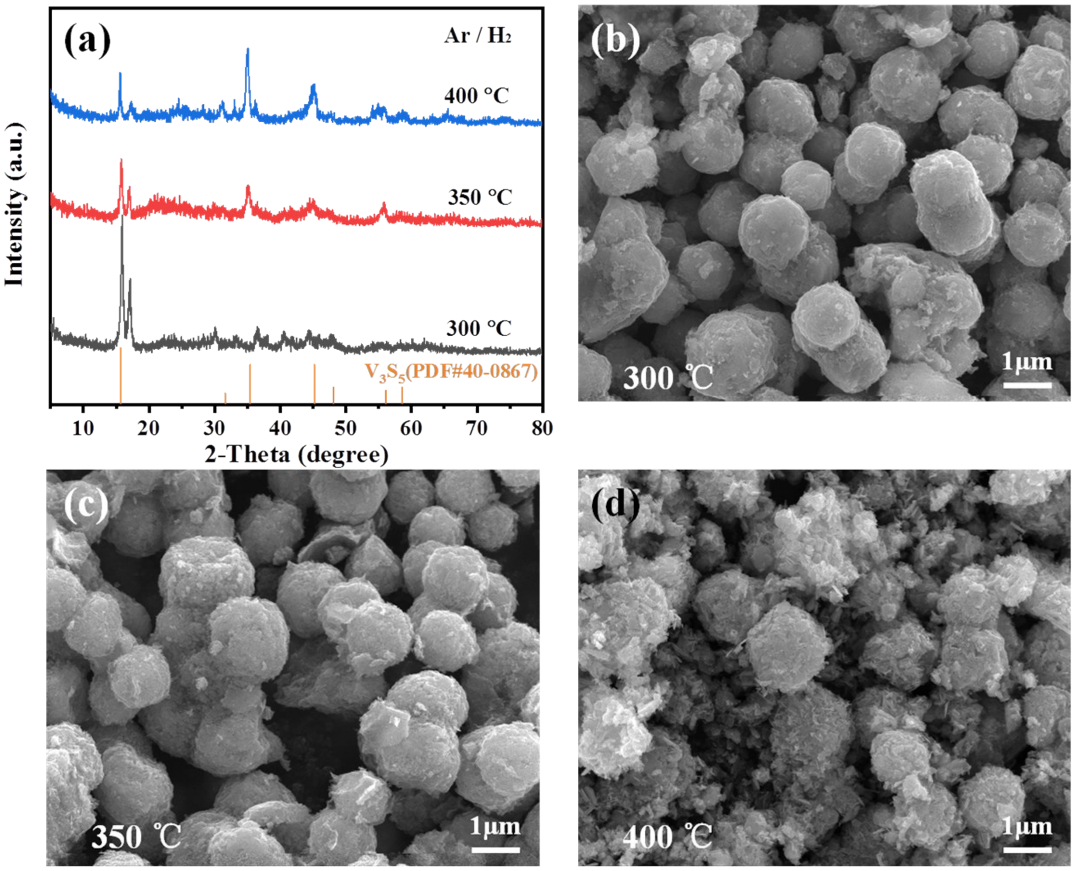

Figure S1. (a) XRD patterns and (b-d) SEM images of the products obtained at different temperatures with the heating rate of 2 °C min^{-1} and the reaction time of 2 h. Of note, consistent with the following SEM analysis results under the argon atmosphere, in the hydrogen/argon mixed atmosphere, when the reaction temperature is not higher than 350 °C, the spherical morphology of the precursor VS_4 can be well maintained.

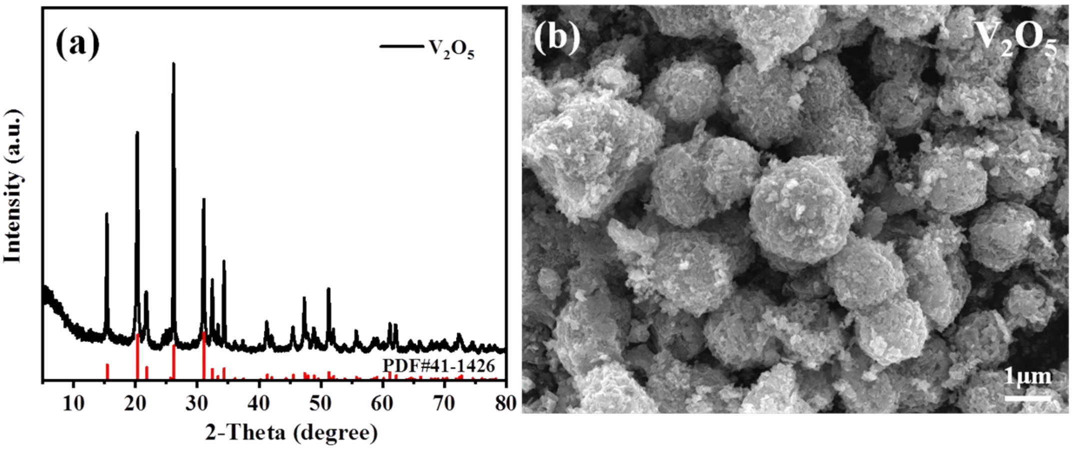

Figure S2. (a) XRD patterns and (b) SEM image of the product obtained at 350 °C for 2 h with the air atmosphere.

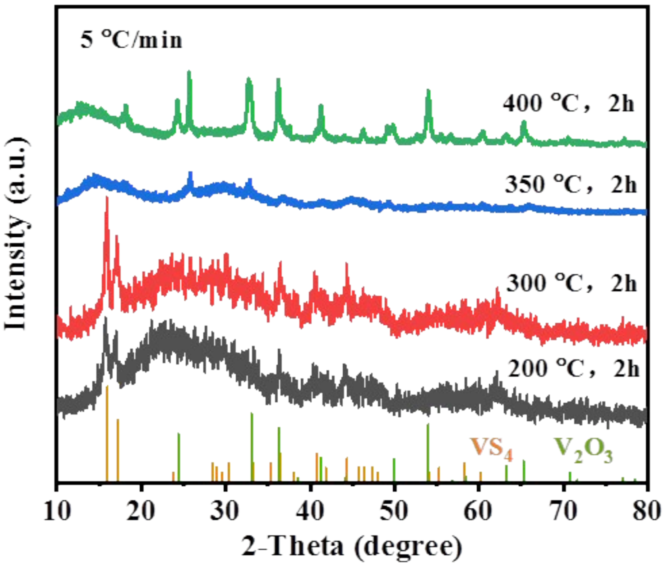

Figure S3. XRD patterns of the products obtained at different temperatures with the heating rate of 5 °C min^{-1} with the argon atmosphere.

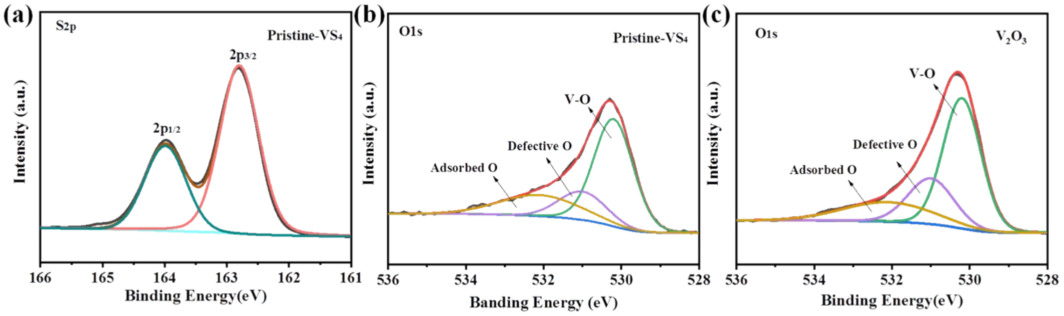

Figure S4. High-resolution S2p (a) and O1s (b) XPS spectra of the precursor $VS_{4.}$ (c)The O1s XPS spectrum of the complete product $V_2O_{3.}$

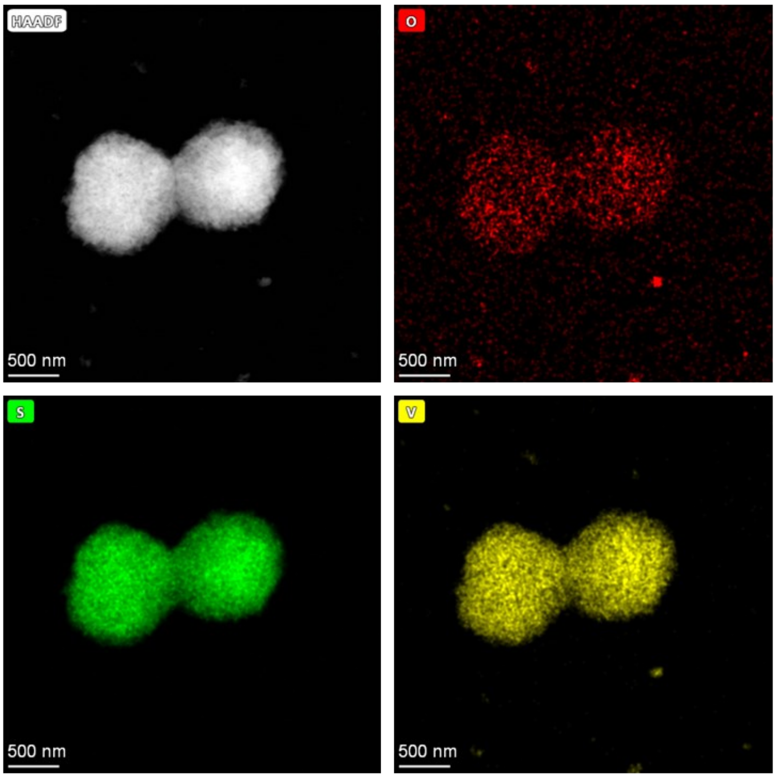

Figure S5. The TEM and the corresponding EDS images of the VS_4/V_2O_3 heterostructure.

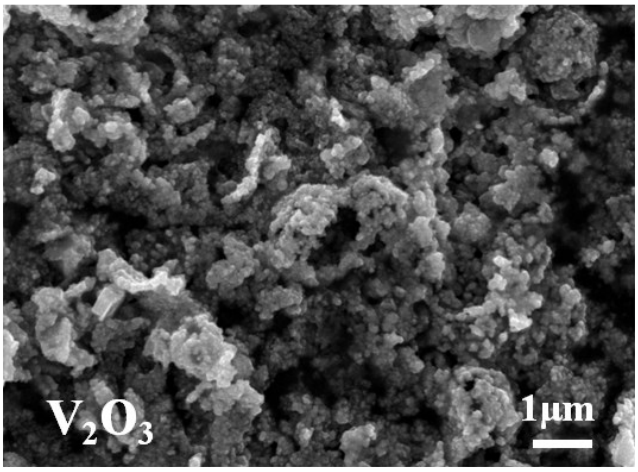

Figure S6. SEM image of the complete conversion product V_2O_3 with the reaction temperature at 400 °C.

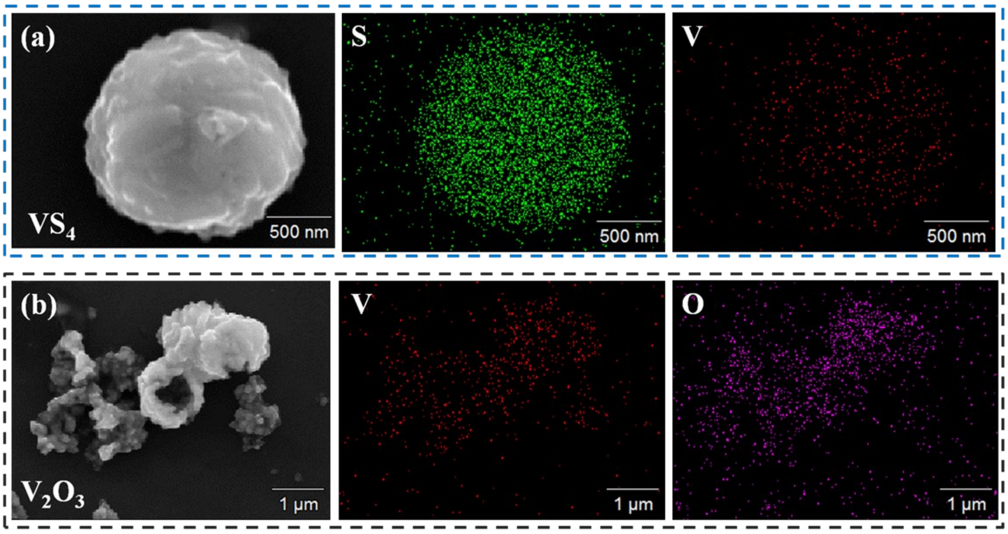

Figure S7. (a) The SEM and the corresponding EDS images of the precursor VS_4. (b)The SEM and the corresponding EDS images of the complete product V_2O_3.

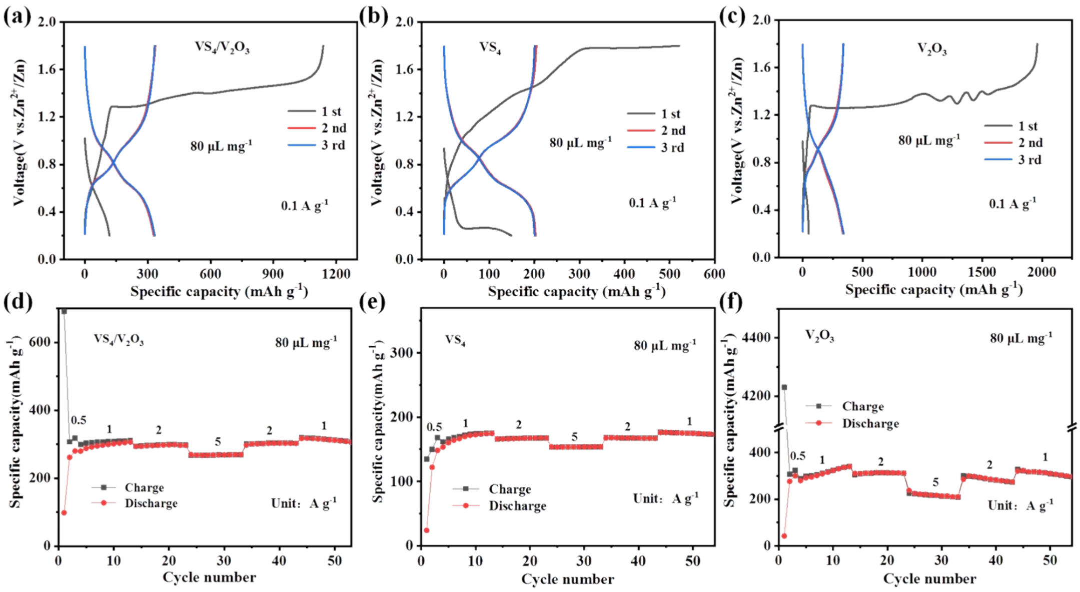

Figure S8. The (a-c) GCD and (d-f) rate performance curves of the VS_4/V_2O_3 heterostructure, the precursor VS_4, and the complete product V_2O_3 with the large voltage range.

A long charging platform will appear at about 1.3 V for the VS_4/V_2O_3 heterostructures, which is similar with the precursor VS_4 and complete product V_2O_3. The above phenomena correspond to the conversion reaction zinc ion storage mechanism of VS_4 and V_2O_3 in the large voltage ranges, and the conversion products are $Zn_3(OH)_2V_2O_7{\cdot}2H_2O$ and V_2O_5, respectively, which have been proved in previous reports.[1, 2] Therefore, in order to prevent the conversion reaction from destroying the structural characteristics of VS_4/V_2O_3 heterostructures, we chose the small (limited) voltage range for zinc ion storage.

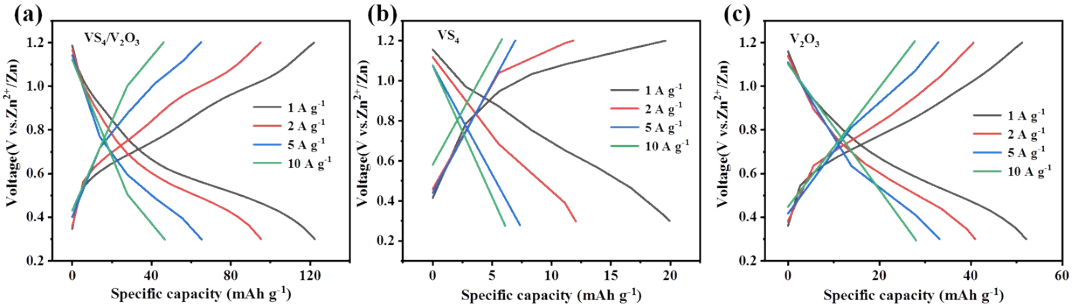

Figure S9. (a-c) Rate performances of the VS_4/V_2O_3 heterostructure, the precursor VS_4, and the complete product V_2O_3, respectively with the electrolyte/active material ratio of 80 μL mg^{-1}.

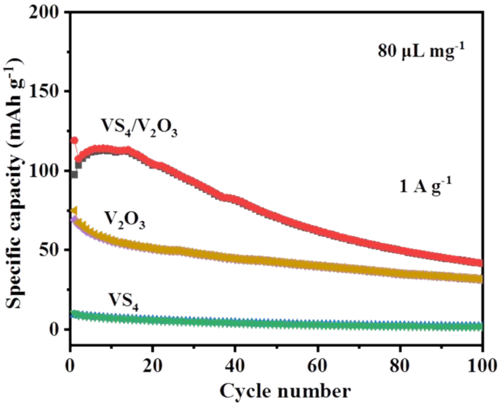

Figure S10. Cycling stability performances of the VS_4/V_2O_3 heterostructure, the precursor VS_4, and the complete product V_2O_3 with the electrolyte/active material ratio of 80 μL mg^{-1}.

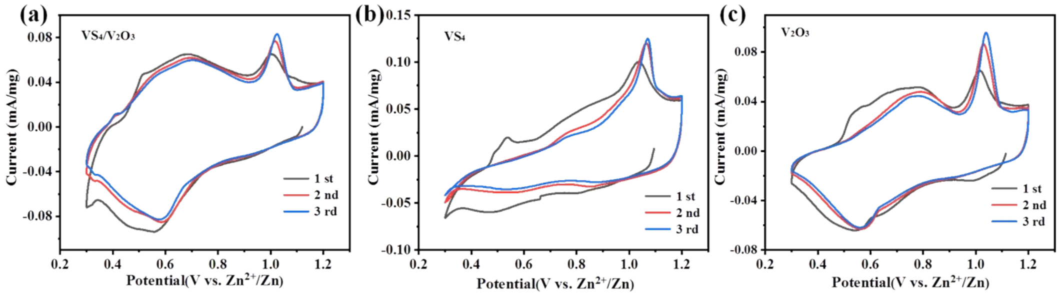

Figure S11. (a-c) The CV curves of the VS_4/V_2O_3 heterostructure, the precursor VS_4, and the complete product V_2O_3, respectively.

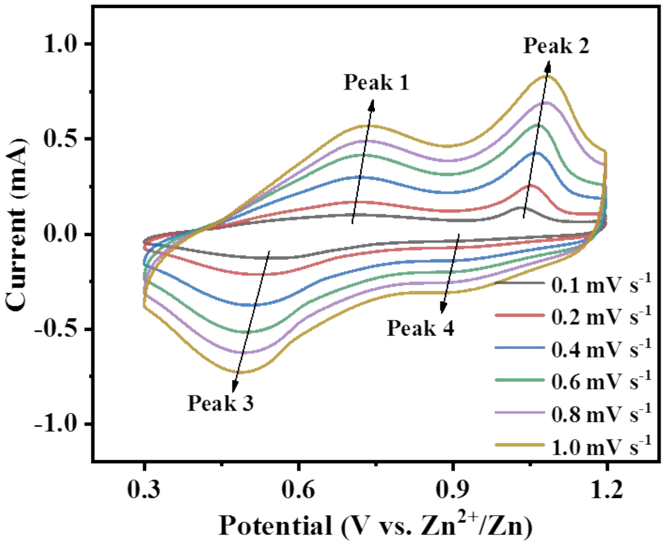

Figure S12. CV curves at different scan rates of the VS_4/V_2O_3 heterostructure.

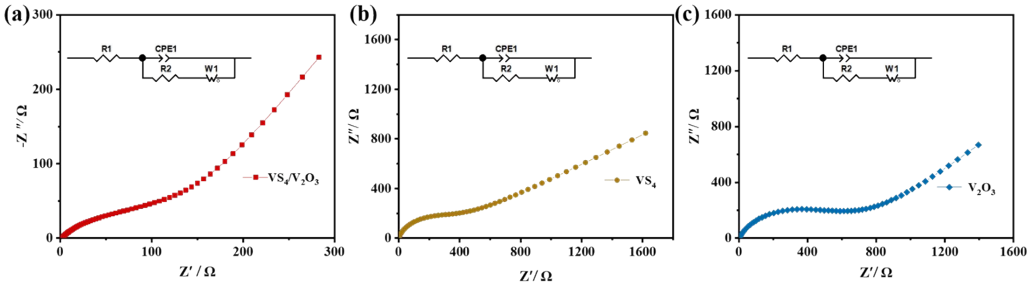

Figure S13. Electrochemical impedance spectra of (a) the VS_4/V_2O_3 heterostructure, (b) the precursor VS_4, and (c) the complete product V_2O_3. Inset: the equivalent circuit (R_1: solution resistance; R_2: charge-transfer resistance; CPE1: constant-phase element; W1: Warburg diffusion process). The charge-transfer resistances of the VS_4/V_2O_3 heterostructure, the precursor VS_4 and the complete product V_2O_3 are 65, 266, and 376 Ω, respectively.

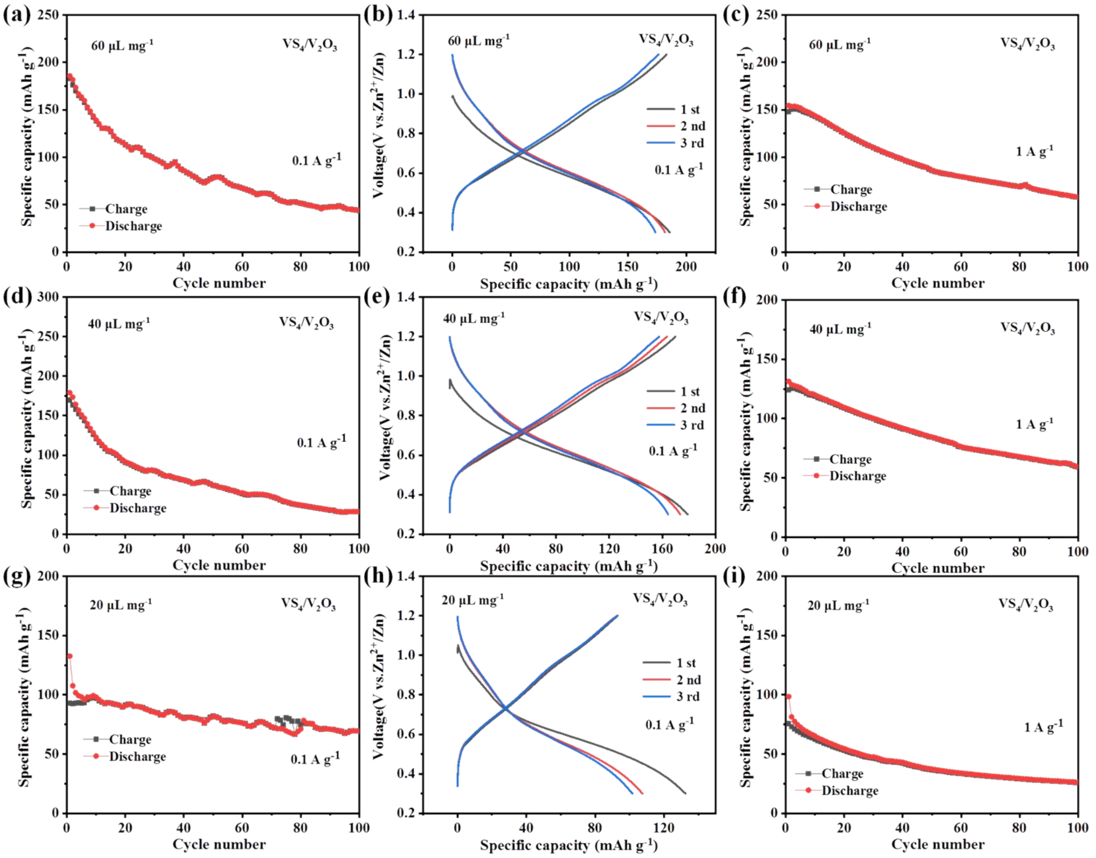

Figure S14. The cycling stability of VS_4/V_2O_3 heterostructures at current densities of 0.1 and 1 A g^{-1} with different electrolyte/active material ratios.

The battery capacity attenuation weakened as the electrolyte/active material ratio decreases to 60 and 40 μL mg^{-1}, but too little electrolyte of 20 μL mg^{-1} leads to the significant decrease of zinc storage capacity. Considering the conventional zinc-ion battery electrolytes contain a large amount of free water resulting in the issues of vanadium dissolution and limited voltage range, the zinc storage merit of VS_4/V_2O_3 heterostructures cannot be fully exploited for the currently applied voltage range and electrolyte system.

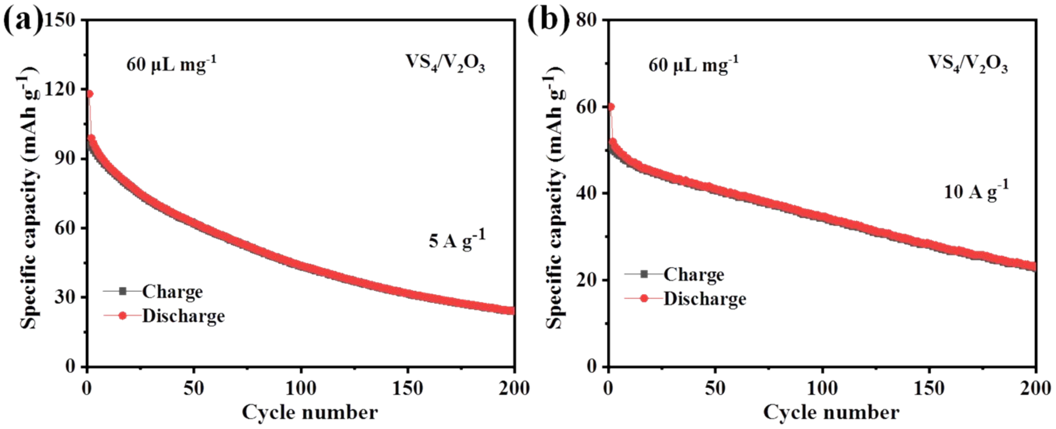

Figure S15. The cycling stability of VS_4/V_2O_3 heterostructures at current densities of 5 and 10 A g^{-1}.

There are many new-type electrolytes such as the highly concentrated[3] and all solid-state electrolytes[4] with the limited free water and the large stable voltage range. Applying the new-type electrolytes, the vanadium dissolution and conversion reaction of VS_4/V_2O_3 heterostructures should be effectively suppressed. Meanwhile, in order to further improve the battery performance of VS_4/V_2O_3 heterostructures, the modify approaches such as carbon framework and vacancy pre-introduction are also the valid strategies.[5, 6]

Therefore, given that the heterostructure has abundant interfaces and grain boundaries, we believe that the structural advantages of VS_4/V_2O_3 heterostructures for the high-performance zinc storage can be achieve via applying the new-type electrolyte and the modify strategy in our follow-up research.

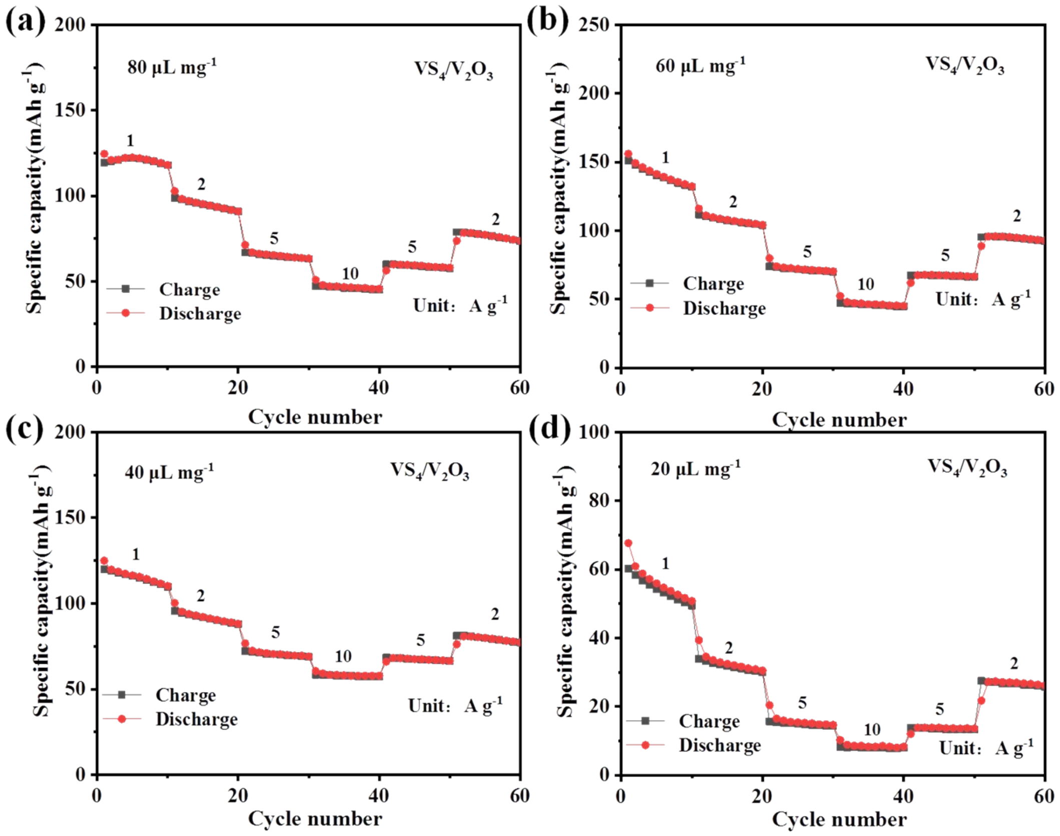

Figure S16. Rate performances of VS_4/V_2O_3 heterostructures with different electrolyte/active material ratios. The improved rate performance was achieved via applying the electrolyte/active material ratio of 60 μL mg^{-1} comparable with the initial 80 μL mg^{-1}. At the current densities of 1, 2, 5 and 10 A g^{-1}, the improved zinc storage capacities can reach 148, 110, 74 and 48 mAh g^{-1}, respectively. We believe that the enough rate performance can be achieved via applying the optimal new-type electrolyte and the modify strategy via solving the high-potential conversion and vanadium dissolution challenges in our follow-up research.

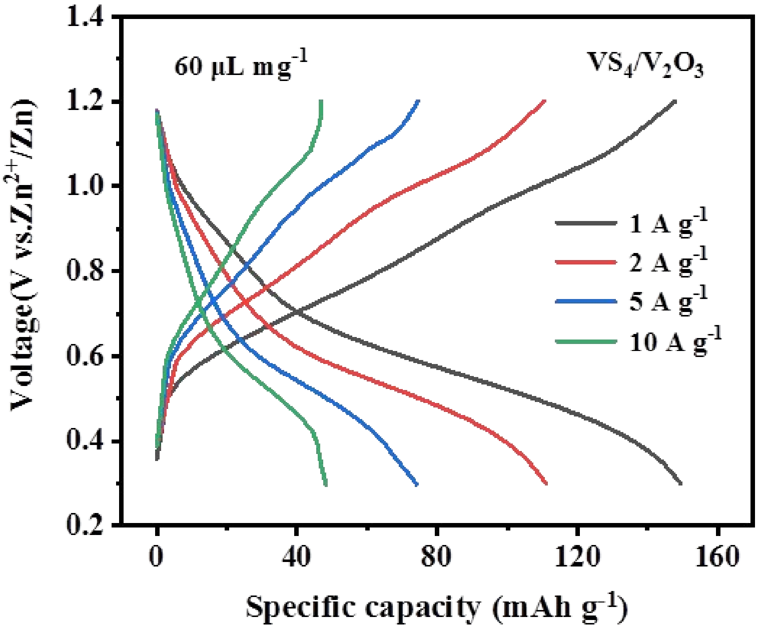

Figure S17. The improved voltage-capacity curves of the VS_4/V_2O_3 heterostructure at different current densities with the electrolyte/active material ratio of 60 μL mg^{-1}.

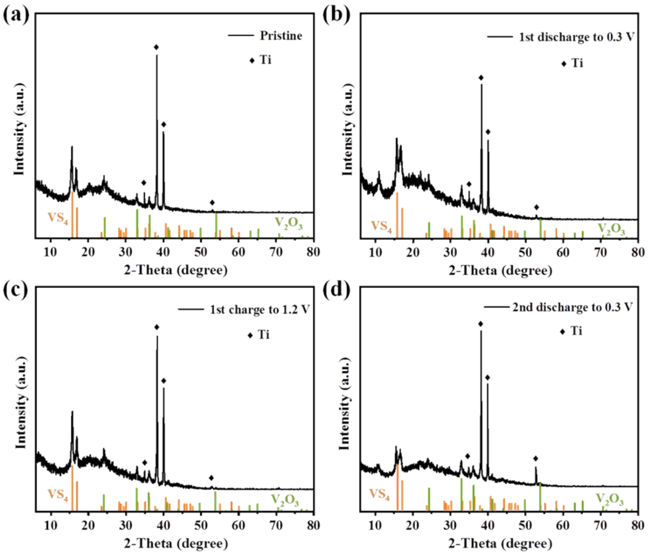

Figure S18. XRD patterns of the VS_4/V_2O_3 heterostructure electrodes at (a) the pristine, (b) the firstly full discharging, (c) the firstly full charging, and (d) the secondly discharging states. It should be noted that the peaks appeared at 34.9°, 38.2°, 40.3°, and 53.0° are attributed to the titanium foil (current collector).

The XRD test was first applied to uncover the phase composition evolution of the VS_4/V_2O_3 heterostructures during zinc ion storage. At the pristine state, there are two strongest diffraction peaks at 15.8° and 16.8° attributed to (011) and (020) crystal planes of VS_4, respectively. Meanwhile, there are three characteristic peaks at 24.2°, 32.9°, and 36.3°, which are consistent with the crystal plans (012), (104), and (110) of V_2O_3, respectively. For the first full discharging state, all the crystal plane peaks of VS_4/V_2O_3 heterostructures still exist, other than the relative strength change of (011) and (020) crystal planes of VS_4, which demonstrates that the zinc ion storage is not the conversion reaction. When at the first full charging state, all the characteristic peaks of VS_4/V_2O_3 heterostructures go back to the pristine state, indicating the reversible zinc ion storage process. At the secondly full discharging state, the characteristic peaks of VS_4/V_2O_3 heterostructures are similar with the firstly full discharging state, further demonstrating the reversible zinc ion storage. Of note, at the firstly and secondly full discharging states, the new peak at about 11.0° should be attributed to the side-product $Zn_xOTf_y(OH)_{2x-y}\cdot nH_2O$ due to applying the zinc trifluoromethane sulfonate electrolyte.[7]

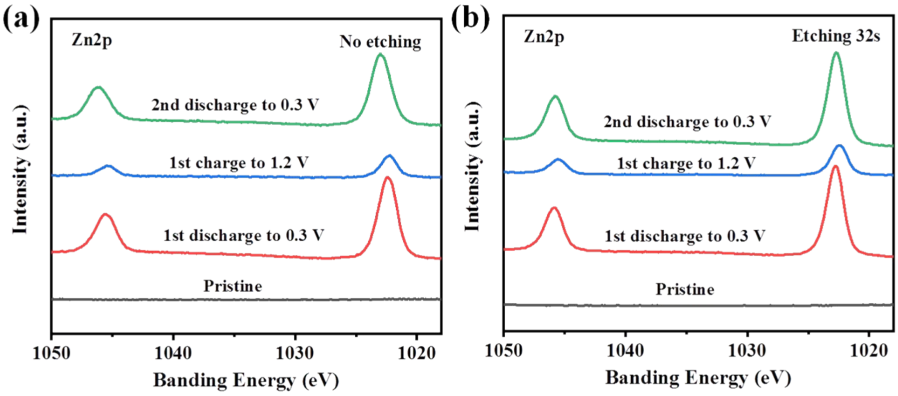

Figure S19. The Zn 2p XPS spectra of the VS_4/V_2O_3 heterostructures at different zinc ion storage states (a) without the argon ion etching (b) and after etching 32s.

The XPS test was carried out to further analysis the valence states and element coupling environments of the VS_4/V_2O_3 heterostructures during zinc ion storage. When firstly discharged to 0.3 V, two obvious peaks of $Zn2p_{3/2}$ (1022.5 eV) and $Zn2p_{1/2}$ (1045.6 eV) appear, indicating that the successful zinc ion storage compared with the pristine state without zinc element signals. Moreover, even after etching 32s via argon ion sputtering during XPS testing process, the zinc element signals can also obviously detect, demonstrating the zinc ions are successfully intercalated in the VS_4/V_2O_3 heterostructures. When firstly charged to 1.2 V, the peak intensities of Zn 2p weaken, indicating the reversible zinc ion deintercalation process.

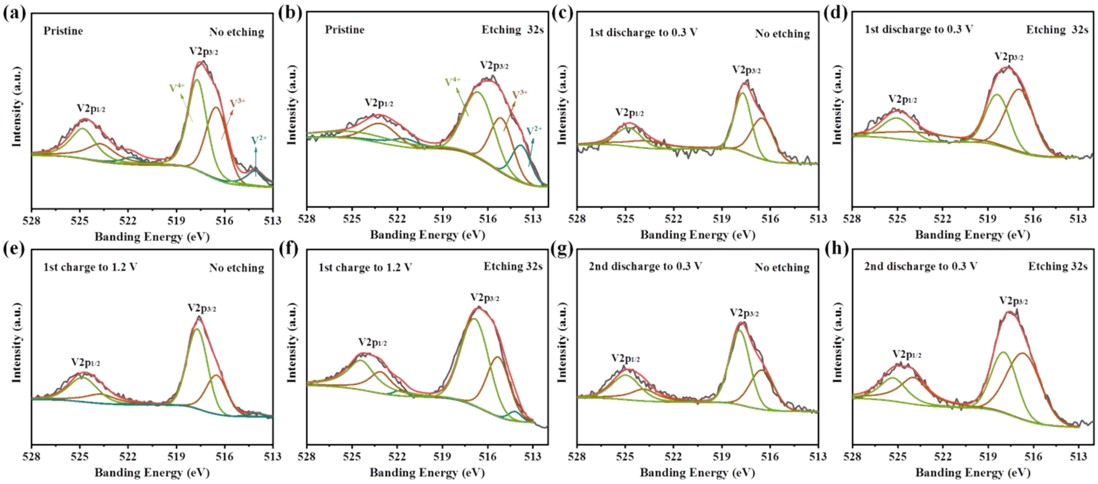

Figure S20. The V2p XPS spectra of the VS_4/V_2O_3 heterostructures at (a, b) the pristine, (c, d) the firstly full discharging, (e, f) the firstly full charging, and (g, h) the secondly discharging states without the argon ion etching and after etching 32s, respectively.

For the V2p XPS spectra of the pristine state VS_4/V_2O_3 heterostructures, at the firstly full discharging state, the peak area proportion corresponding to V^{4+} at about 517.7 eV decreases, and the peak area proportion corresponding to V^{3+} at about 516.5 eV increases, which indicates that a part of V^{4+} undergoes a reduction process during the zinc ion intercalation. Moreover, after the argon ion etching, the partial reduction phenomenon from V^{4+} to V^{3+} is more obvious, further proving the occurrence of zinc ion intercalation. When charged to 1.2 V, the vanadium valances of V^{4+} and V^{3+} are nearly complete recovery especially for the argon ion etching sample, indicating the reversible zinc ion extraction from the VS_4/V_2O_3 heterostructures. For the secondly full discharging state, the vanadium valances of V^{4+} and V^{3+} are similar with those at the firstly full discharging state, demonstrating that the VS_4/V_2O_3 heterostructures can achieve the reversible zinc ion storage. The above BET, CV, XRD, and XPS analyses confirm that the zinc ion storage is the intercalation/deintercalation mechanism for the VS_4/V_2O_3 heterostructures.

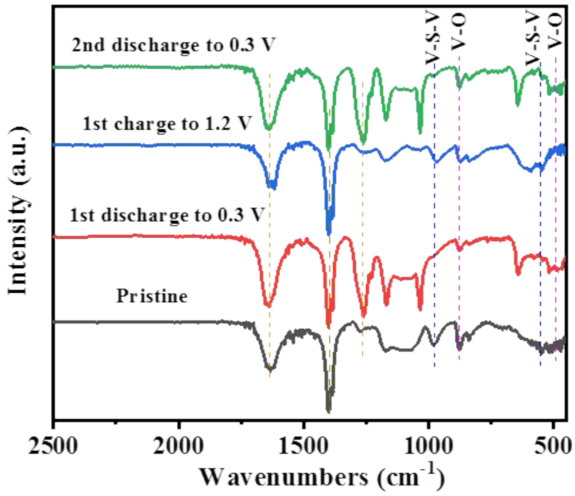

Figure S21. FTIR spectra of the VS_4/V_2O_3 heterostructures at different zinc ion storage states.

The FTIR test was measured to further analyze the structural information evolution of the VS_4/V_2O_3 heterostructures during the zinc ion storage. For the first full discharging state, the characteristic peaks of VS_4/V_2O_3 heterostructures are kept unchanged comparable with the pristine state, indicating the structure stability during zinc ion intercalation. Furthermore, at subsequent full charging/discharging states, the the characteristic peaks of VS_4/V_2O_3 heterostructures are kept stability, revealing that VS_4/V_2O_3 heterostructures can achieve the stable zinc ion intercalation/deintercalation. It's worth noting that the peaks appearing at about 1633 and 1267 cm^{-1} are attributed to the C-O characteristic vibration. The peak at about 1393 cm^{-1} belongs to the characteristic peak of amorphous carbon. The FTIR result is consistent with the above XRD analysis.

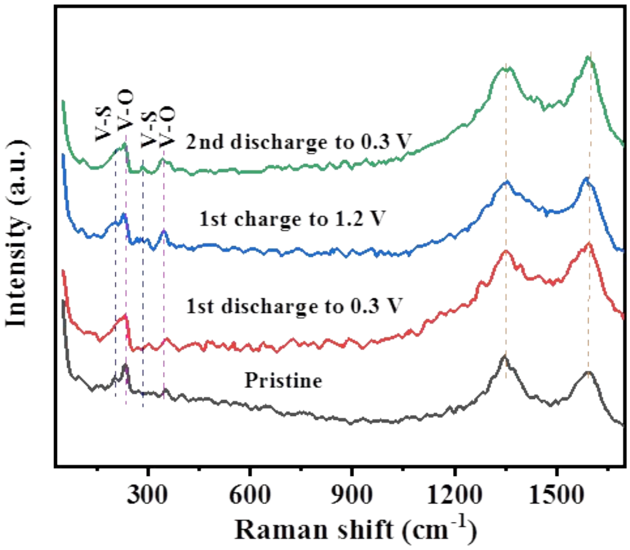

Figure S22. Raman spectra of the VS_4/V_2O_3 heterostructures at different zinc ion storage states.

The Raman spectroscopy was appled to further investigate the microscopic structure evolution of the VS_4/V_2O_3 heterostructures during the zinc ion storage. At different zinc ion storage states, the typical Raman peak is kept unchanged, indicating the structure stability during zinc ion intercalation/deintercalation. Of note, the peaks appearing at 1346 cm^{-1} and 1595 cm^{-1} are attributed to the characteristic peaks of conductivity agent (Super P). Meanwhile, most of Raman modes are relatively weak in intensity due to the scattering of incident light caused by the various components of the tested electrode. The Raman result is consistent with the above XRD, XPS, and FTIR analyses.

References

1 H. Qin, Z. Yang, L. Chen, X. Chen and L. Wang, *J. Mater. Chem. A*, 2018, **6**, 23757-23765.

2 H. Luo, B. Wang, F. Wang, J. Yang, F. Wu, Y. Ning, Y. Zhou, D. Wang, H. Liu and S. Dou, *ACS Nano*, 2020, **14**, 7328-7337.

3 F. Wang, O. Borodin, T. Gao, X. Fan, W. Sun, F. Han, A. Faraone, J. A. Dura, K. Xu and

C. Wang, *Nat. Mater.*, 2018, **17**, 543-549.

4 L. Ma, S. Chen, N. Li, Z. Liu, Z. Tang, J. A. Zapien, S. Chen, J. Fan and C. Zhi, *Adv. Mater.*, 2020, **32**, 1908121.

5 S. Deng, Z. Yuan, Z. Tie, C. Wang, L. Song and Z. Niu, *Angew. Chem. Int. Edit.*, 2020, **59**, 22002-22006.

6 Z. Li, Y. Ren, L. Mo, C. Liu, K. Hsu, Y. Ding, X. Zhang, X. Li, L. Hu, D. Ji and G. Cao, *ACS Nano*, 2020, **14**, 5581-5589.

7 P. Oberholzer, E. Tervoort, A. Bouzid, A. Pasquarello and D. Kundu, *ACS Appl. Mater. Interfaces*, 2019, **11**, 674-682.